Single Crystal Deposition via Wire Arc Additive Manufacturing

A Thesis
Presented in Partial Fulfillment of the Requirements for the
Degree of Master of Science
with a
Major in Mechanical Engineering
in the
College of Graduate Studies
University of Idaho
by
Jacob D. Miller

Major Professor: Michael Maughan, Ph.D., PE
Committee Members: Indrajit Charit, Ph.D., PE; Krishnan Raja, Ph.D., PE
Department Administrator: Gabriel Potirniche, Ph.D., PE

December 2020

Authorization to Submit Thesis

This thesis of Jacob D. Miller, submitted for the degree of Master of Science with a Major in Mechanical Engineering and titled "Single Crystal Deposition via Wire Arc Additive Manufacturing," has been reviewed in final form. Permission, as indicated by the signatures and dates below, is now granted to submit final copies to the College of Graduate Studies for approval.

Major Professor: _____ Date: _____
Michael Maughan, Ph.D., PE

Committee Members: _____ Date: _____
Indrajit Charit, Ph.D., PE

_____ Date: _____
Krishnan Raja, Ph.D., PE

Department Administrator: _____ Date: _____
Gabriel Potirniche, Ph.D., PE

Abstract

The rapidly evolving field of additive manufacturing has developed from a niche manufacturing technique to a rapidly evolving manufacturing technique. The ability to manufacture complex geometries in addition to reduction in wasted materials common to subtractive manufacturing techniques has led to further inquiry not only in deposition methods but materials as well. One material that is currently manufactured at high expense are single crystal components.

Single crystal components are typically subjected to harsh environments including high thermal exposure and repeated stress. The boundary-free lattice structure of a single crystal is ideal in these situations due to its high resistance to creep and fatigue crack growth. Current methods of manufacturing these components involve highly controlled directional solidification, a time and material costly procedure. The objective of this study is to investigate the feasibility of additively manufacturing single crystal components via Wire Arc Additive Manufacturing (WAAM) and with a variation of the Tungsten Inert Gas (TIG) process. WAAM tests were conducted using the University of Idaho's WAAM machine, VandalForge, as well with the TIG variant. Material was deposited first onto an ultra-pure zone refined single crystal ingot for feasibility validation and then onto a 99.995% pure single crystal substrate oriented in the <111> direction.

Once deposits were made onto the substrates, samples were cold mounted in epoxy, polished and etched using Marble's reagent. Optical Microscopy (OM) provided distinct images of segregated grain boundaries, however samples were also mapped with EBSD to confirm the effectiveness of the etchant for pure nickel grain boundaries. Further analysis of both OM and EBSD yielded that single crystal regions of deposited material had formed on the substrate.

Acknowledgements

I would like to express my gratitude towards Dr. Michael Maughan, my major professor, for his support, patience, and advice on this project. I would also like to thank Dr. Krishnan Raja and Dr. Indrajit Charit for supporting this research and providing valuable insight in both the thesis as well as my final defense.

Thanks to all of the professors, faculty and staff at the University of Idaho for providing so many educational opportunities and wise insight.

Thanks also to my fellow undergraduate and graduate students that I have had the pleasure of studying alongside and working with during my studies.

Dedication

This thesis is dedicated to all family and friends that have supported and pushed me to always do my best, especially my mother, Jennifer, my sister, Sarah, and my father, Doug.

Table of Contents

List of Tables

List of Figures

Chapter 1: Introduction

Recent advancements in material selection and fabrication have yielded increasing efficiencies and performance of components subjected to harsh environments such as high temperatures and cyclic loading under high stresses as in the turbine industry. Many turbine blades are manufactured out of single-crystal nickel superalloys due to their high temperature tolerances as well as resistance to crack growth in situations where creep-fatigue growth is prevalent. Currently, most manufacturing processes for single crystal components stem from directional solidification, a highly controlled casting process that is time and energy consumptive. When these components do develop damage, many times they are scrapped and replaced with brand new parts.

Additive manufacturing is a rapidly evolving field that is attractive not only due to the complex geometries that are attainable only by manufacturing in the layer-by-layer process, but as well as for the reduction in scrap material that is a byproduct of traditional manufacturing processes such as subtractive manufacturing. Recent developments in additive manufacturing processes have included a broad scope of materials to be deposited, including but not limited to traditional plastics, wood fibers, and metals. Current methods of metallic additive manufacturing vary, but many involve layering finely deposited material and remain a relatively expensive method of manufacturing.

Wire Arc Additive manufacturing (WAAM) is able to achieve deposition rates significantly higher than other methods of metal additive manufacturing without the use of overly expensive equipment or highly regulated environments. A spinoff of the popular Metal Inert Gas (MIG) welding process, there is much industry knowledge of how to create strong welds as well as material compatibility and heat affected zone (HAZ) control. Higher rates of deposition also make WAAM an attractive option to create components in a relatively short time frame that have acceptable strength and require minimal post process machining to fulfill dimensional tolerances.

This study analyzes the feasibility of depositing pure nickel onto a pure nickel single crystal substrate and having the deposited material assume the same microstructure as that of the substrate, essentially additively manufacturing single crystal components. Initial tests were conducted using a WAAM system, however a Tungsten Inert Gas (TIG) variant was also studied due to a more precise control of heat input as well as arc control, mimicking the same solidification control as that of directional solidification.

Chapter 2: Background

2.1 Single Crystal Applications

Single crystal materials have unique properties that make them highly desirable in niche applications. Due to the strict order of the atomic arrangement, the entire crystal lattice is continuous and unbroken by grain boundaries, making the material one large grain. As grain boundaries are regions of materials that are especially susceptible to defects, corrosion, and the ability for creep fatigue crack growth to occur, single crystallinity leads to many unique mechanical, optical, and electrical properties that allow for precision and performance unmatched by traditionally produced materials [1].

One of the biggest uses for single crystal metallic components is for turbine blades in jet engine components. These components are commonly subjected to extreme heat and stresses, with normal operating temperatures around 1650°C for commercial engines with the turbine rotating at around 12,000 rpm and an expected lifespan of 25,000 hours on average [1]. In early stages of engine development, turbine blades were conventionally cast having an equiaxed microstructure. These blades were especially susceptible to intergranular cavitation, increase of chemical activity, and boundary slipping, which in turn lead to creep and corrosion failures. While these result from the high temperatures and stresses, engines must run at higher temperatures to maintain optimal efficiencies, leaving material enhancement the chosen approach [2].

With the development of casting processes for single crystal components as well as the improvements in new materials with varying chemical compositions, turbine blades have been able to far exceed their predecessor's performance standards. Modern single crystal turbines are shown to have nine times the relative lifespan of equiaxed blades as well as three times the corrosion resistance lifespan [2]. In addition to these mechanical and chemical strengthening factors, higher melting temperatures allow for larger, more efficient gas turbines.

2.2 Current Manufacturing Practices for Single Crystals

Current industry standards for manufacturing large single crystal components rely heavily on controlled solidification and cooling processes in order to maintain a defect-free lattice. These methods are time-costly and have remained relatively unchanged in the metallurgical field since the 1970's [2].

Directional Solidification of Cast Metals

Current manufacturing processes of metallurgical single crystal manufacturing primarily stem from the concept of directional solidification. In this method, molten metal is poured into a cast with a seed crystal at the bottom of the casting. Once the metal is poured, the base of the casting closest to the seed crystal is slowly lowered into a cooling region, promoting slow solidification from the bottom of the casting towards the direction of the sprue. Figure 2.2.1 illustrates a typical directional solidification process.

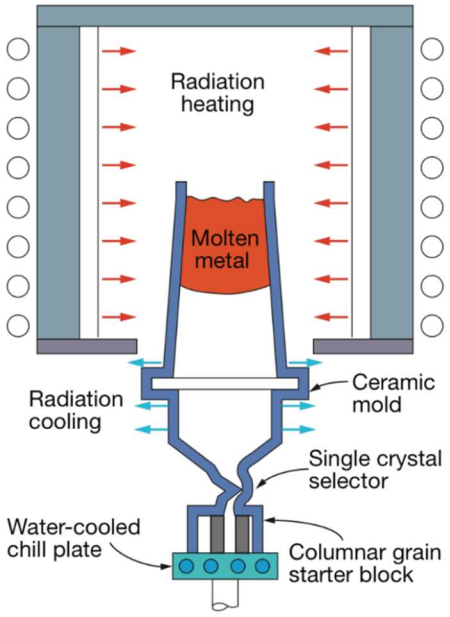

Figure 2.2.1: Directional solidification process including single crystal selector and seed crystal (starter block) [2].

Grains initially form in the orientation of the seed crystal or starter block due to a mechanism known as epitaxy, in which the deposited atoms align with the structure of the substrate [3]. From there, grains will continue to grow in the same orientation until competition from other grain boundaries is introduced. In directional solidification apparatuses, there is often a narrow or helical channel directly above the seed crystal that forces differently oriented grains to compete for the preferred direction. This grain competition results in one orientation to form out of the single crystal selection region of Figure 2.2.1 for the casting to grow on. Often, a spiral geometry as shown in Figure 2.2.2 is used for grain selection to promote grain competition.

Figure 1.2.2: Helical grain selector (pigtail) of directional solidification process. Bottom of the selector starts with diverse grain orientation, towards the top grain competition results in a single grain for casting to grow on [2].

Czochralski Method

While the methods of manufacturing metallic single crystals are primarily consolidated to a variation of directional solidification, there is also an extensive array of methods available to nonmetallic materials. Nonmetallic single crystals are highly desirable in the semiconductor, electronics, and optical fields as the lack of impurities allows for consistent material properties that are easily identifiable [2]. The Czochralski (CZ) method is an approach for making large crystal specimens, called boules, at the relatively rapid pace of 10 mm/hour vertically. This process uses a seed crystal that is dipped into molten material and drawn upwards slowly, allowing the molten material to solidify while still connected to the seed material [4]. Figure 2.2.3 illustrates a conventional CZ apparatus for forming large boules of single crystals.

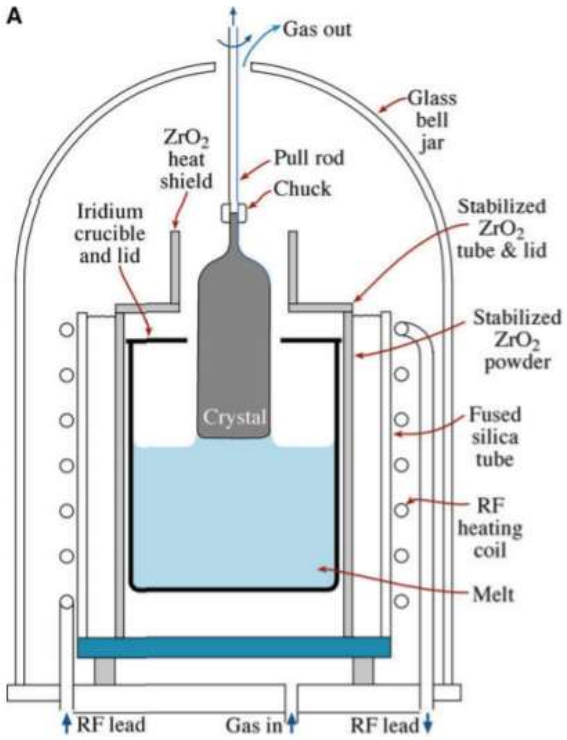

Figure 2.2.3. Cz process diagram. Seed crystal is dipped into molten material and slowly drawn out allowing melted material to solidify to crystal for continuous growth [4].

It can be show that for this process, the maximum possible growth rate of the crystal is the maximum retraction rate of the boule from the molten material [4]:

$$\left(\frac{dx}{dt}\right)_{max} = \frac{1}{\rho_s \Delta H_{fus}}\left[\frac{k_s dT}{dx_s}\right] \tag{1}$$

Where ρ_s is the density of the solid crystal, H_{fus} is the enthalpy of fusion of the material, k_s is the thermal conductivity of the material, and $\frac{dT}{dx_s}$ is the temperature gradient between the liquid-solid interface. Anything beyond this rate of extraction causes supercooling of the extracted material leading to defects as well as the potential for separation between the seed crystal and the molten material. While this method is effective for producing nonmetallic single crystals, the density of molten metals severely limits the extraction rate [4].

Solidification Morphologies

In addition to process limitations in creating single crystal specimens, there are also governing relationships that dictate solidification morphologies such as temperature gradient and

solidification rate that have lent themselves to predicting microstructures present given process parameters.

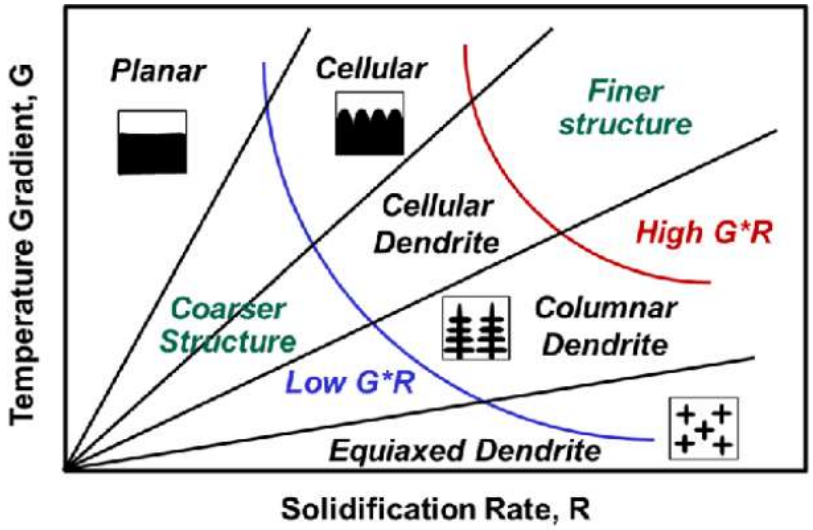

Figure 2.2.4. Predicted solidification morphologies dependent on solidification rate and temperature gradient [5].

Figure 2.2.4 illustrates the dependency of morphologies on both the solidification rate R and the temperature gradient G. Studies similar to the one performed by Lee et al. [5] use this relationship to help define weld pool characteristics and predict microstructure, however there is a consensus on the fact that weld pools have many variables affecting the outcome of the welds such as convection currents in the metal and surface tension of the molten metal and numerical simulation is often used to compare to experimental results for predicting microstructure with varying degrees of error [5].

2.3 Microstructure of Welds

Due to the process of solidification of molten metal onto a solid substrate, welding microstructures are often compared to casting processes, with similar microstructual evolutions present. Unlike casting processes, welds are subjected to extremely elevated cooling rates on the order of 1000 K/s due to high local temperature gradients and high thermal conductivity of metals that lead to high variation in microstructure relative to the proximity of heat input [6],[7].

Welding Zones

Welding regions of interest are typically segregated into different areas by the degree of activity that occurs during the welding process. The substrate is simply the base material onto which the foreign metal is deposited. The heat affected zone (HAZ) is the region of metal that

undergoes a thermal cycle in the presence of the heat input of the welding process, but is still made up solely of the original base material. The HAZ is a region of interest due to the fact that all affected materials in the region tend to re-form unwanted precipitates causing loss in ductility or strength after being exposed to elevated temperatures [8].

The fusion zone is where deposited material meets the substrate, with the partially melted substrate in this region interacting with the molten deposit to form an atomically close bond to the existing substrate [9]. This zone typically cools with similar microstructures as would be expected in a casting due to the molten nature of the material in this area with the substrate acting as a mold, guiding solidification parameters similar to casting processes [6]. This microstructure consists of strong columnar epitaxial growth nearest to the fusion zone, where the temperature gradient is the highest and solidification rate is the slowest. Nearer to the surface of the weld, it is more common to observe an equiaxed microstructure due to factors such as cooling of the weld via the inert gas shield or nucleation of grain sites due to dendrite fragmentation on the surface of the weld [10]. Figure 2.3.1 illustrates the interaction between deposited material and substrate.

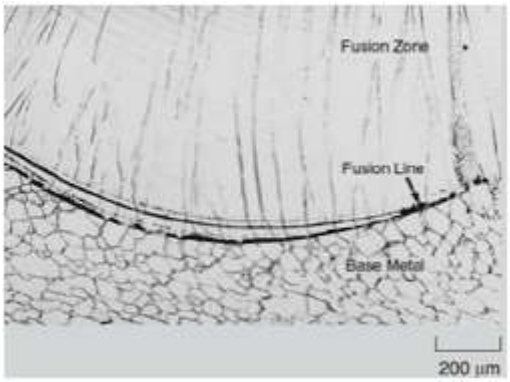

Figure 2.3.1. Optical microscopy depicting the Substrate, Fusion Line, and Fusion Zone in a weld. Columnar grains appear to grow epitaxially from the base metal, a common trait for welds [10].

Constitutional Supercooling

While directional solidification fundamentally relies on the direction of solidification, another critical heavy influence on the microstructure of the cast components is the solidification rate. In alloyed materials such as the nickel superalloys that turbine blades are commonly composed of, solidification rate plays a large role on the homogeneity of the grain structure due to the principle of constitutional supercooling. In a heterogenous material that is in a liquidous phase, the constituents of the material have varying freezing points. Rapid advancement of the

solidification front can lead to nucleation of constituents with higher melting temperatures ahead of the solidification front, allowing sites for new grain orientations to originate [4]. Stable planar solidification is critical for single crystal growth to ensure crystallization occurs uniformly and there are no competing grain boundaries as the solidification front progresses. The general governing equation for stable planar solidification of an alloy follows the equation:

$$\frac{G_L}{R} > \frac{\Delta T_o}{D_L} \tag{2}$$

Where G_L is the temperature gradient of the liquid, R is the solidification front growth rate, ΔT_o is the equilibrium solidification temperature range for a given composition, and D_L is the solute diffusion coefficient in the liquid [10]. When this equality holds true, the planar solidification front will be stable and planar growth is possible. However, when this inequality does not hold true, supercooling will cause nucleation ahead of the solidification front and allow for spontaneous grain growth to occur in a non-planar fashion. Figure 2.3.2 is a graphical representation of constitutional supercooling, in which a solidification rated denoted by T_L that is lower than the critical gradient based on the composition of the alloy leads to a region of supercooling, where solidification of constituents with higher melting temperatures can occur ahead of the solidification front due to the slower overall rate of solidification.

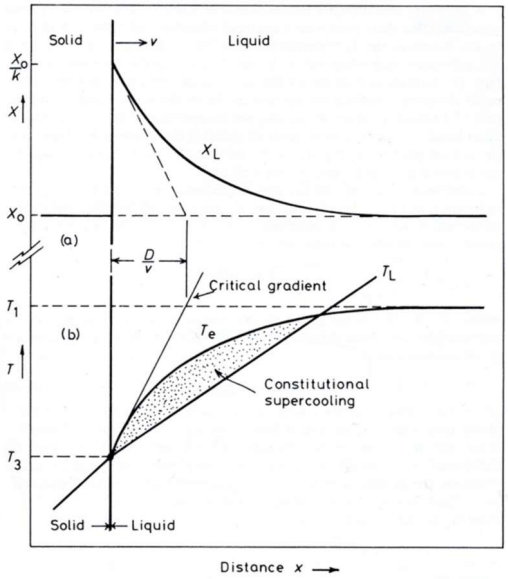

Figure 2.3.2: Diagram depicting region of supercooling for advancing solidification front based on equilibrium temperatures for a binary alloy [10].

In Directional Solidification procedures, supercooling can be avoided because the temperature gradient can be driven very high by cooling plates as depicted in Figure 1 and the solidification rate can be slowed by slowing the rate of extraction of the casting from the oven. However, the rapid solidification rates associated with welding procedures leads to nickel-based superalloys being extremely prone to stray grain formations [10].

2.4 WAAM

Wire Arc Additive Manufacturing (WAAM) utilizes the traditional MIG welding processes to deposit material while the torch is positioned and moved by either a robotic manipulator or a gantry system common to other methods of additive manufacturing. The MIG technique is highly advantageous due to the simplicity of setup, capital cost, and reliability of being able to produce high quality welds within a relatively large window of parameters.

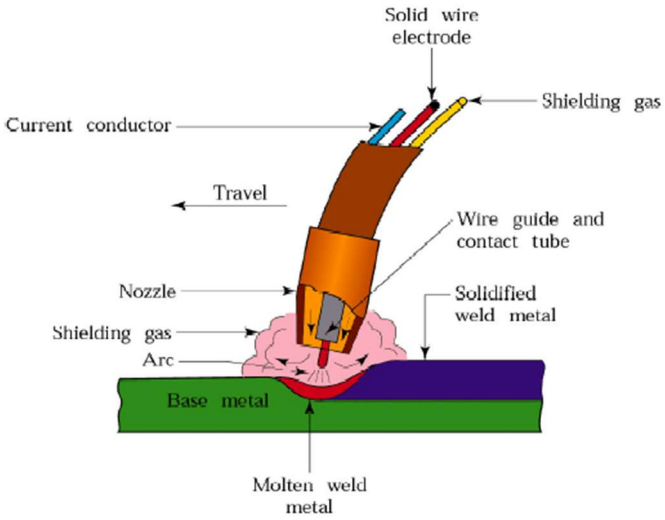

Figure 2.4.1: Traditional MIG welding diagram, with solid wire as both the consumable electrode and the filler material [9].

The MIG process is a derivative of Gas Metal Arc Welding (GMAW) that involves the feed wire acting as both deposit material and a consumable electrode. Figure 2.4.1 illustrates the components of the GMAW process. The TIG process is a derivative of Gas Tungsten Arc Welding (GTAW) that provides a more consistent arc and higher control of heat input due to the fact that the electrode is a tungsten rod that is not consumable and wire or powder is fed into the arc from an external feed. One of the fundamental attributes of MIG welding that is also highly revered in the field of additive manufacturing is the high rates of deposition that are achievable when compared to other methods of metallic additive manufacturing. WAAM can achieve rates of 1-4 kg/h depending on the material deposited [11]. These higher deposition rates provide the

capability of manufacturing large metallic components in relatively short amounts of time with a substantial decrease in wasted materials compared to other types of metal AM or subtractive manufacturing. However, the cost of these benefits is lower resolution, with WAAM components requiring some finishing machining. In addition to requiring post-processing machining, WAAM can also introduce high amounts of residual stresses in components due to the large amount of localized heat input required to achieve fusion of deposited material. This causes some materials to require Post Weld Heat Treatment (PWHT) in order to relax residual stresses as well as deformation [8,11].

2.5 Previous Works

While there is a plethora of literature available on the optimization parameters of WAAM systems as well as the formation of single crystals via directional solidification, there is little research available at the intersection of the two.

Ordinarily, to enhance the performance of AM components a primarily equiaxed microstructure is sought to mimic the microstructure of wrought materials. Prado-Cerqueira et al. analyzed favorable processing parameters for WAAM of thin walled mild steel components utilizing a GMAW system coupled with a Cold Metal Transfer (CMT) mechanism to achieve optimal physical properties such as hardness and tensile strength of deposits [12]. This study focused on varying the thermal input, measured in Joules per millimeter, and observing the change in physical properties that resulted. The thermal input in this study was calculated as follows:

$$TI = \frac{V * I * \mu}{travel\ speed} \tag{3}$$

Where V is the arc voltage, I is the current, μ is a constant coefficient for the welding process used, and travel speed is in mm/s. The results of this study depict that processes with the highest thermal input resulted in higher hardness values, which can also be associated with finer microstructures [13].

Basak et al. conducted research in the field of additive manufacturing of single crystal components with CMSX-4 via Scanning Laser Epitaxy, a common method of depositing material at relatively low rates with highly localized heat input [14]. They showed that CMSX-4 powder could be deposited onto a single crystal substrate demonstrating epitaxial growth, however dendritic formation was still present although refined compared to previous studies. One

interesting thing about this study, however, was that multiple passes over deposited materials with the heat source helped refine the microstructure to the desired qualities. This can be attributed to the beam providing large amounts of heat in forms mimicking high amounts of both pre- and post-weld heat treatments, which allows for a slower solidification rate while maintaining a high thermal gradient, as well as allowing for dislocations to settle out of the matrix [8,14].

In their study of nickel superalloys varying rapid solidification parameters, Fu et al. established an experimental procedure to determine the effects of rapid solidification on microstructure of alloys [15]. High rate directional solidification is defined as having a cooling rate on the order of 1-10^3 K/s, while traditional directional solidification procedures are restricted to cooling rates on the order of 1 K/s. This study manipulated cooling rate by altering the temperature gradient in a directional solidification device between 250 K/cm to 1300 K/cm and studied the effects of solidification rate on resulting microstructure. This study uses the supercooling relationship discussed in Section 2.2.2, and results indicate typical supercooling phenomena are still present even at rapid solidification rates. A higher $\frac{G}{R}$ yielded a transition from cellular growth to a planar front, as well as displaying more even diffusion γ' precipitates leading to enhanced mechanical properties in rupture life tests at 1050°C and 160Mpa. While this study still uses traditional directional solidification practices, the order of magnitude of the solidification rate is significantly higher than common practices previously analyzed, approaching solidification rates seen in welding practices [8].

Chapter 3: Methods

This study utilized a thermal study conducted in SolidWorks, experiments, and EBSD analysis of experimental results to verify the feasibility of depositing single crystal material onto a single crystal substrate. A small amount of experimental substrate was available, therefore extensive initial testing was performed to obtain parameters for WAAM machines that yielded optimal welding conditions. Numerical analysis was also performed to gain an understanding into the thermal flow of the system and ensure directional solidification characteristics would be present on a macroscopic scale. The thermal simulation of welding processes has been extensively conducted with many models specific to the material being welded, the equipment used to weld, and the operating parameters for the equipment being used in the studies [8,15,18]. Due to the high variability in alloy compositions, convective fluid flow of the weld pool, and substantial amounts of other factors from previous research, initial experiments in this study were carried out in the form of spot welds over a fixed location in order to determine solidification characteristics of Ni-200 substrate and deposited material. The use of Ni-200 effectively eliminates the aspect of supercooling as it is commercially pure nickel and the absence of alloying elements allows for the analysis to become greatly simplified.

3.1 Numerical Analysis

Prior to depositing material onto substrates, a thermal simulation was conducted using the Solidworks thermal simulation package. The purpose of this analysis was to determine the rate of heat transfer from conductive, radiative, and convectional cooling across a deposited bead of metal immediately following the extinguishing of the arc. The ideal scenario for solidification of the bead would be most of the cooling to occur from the substrate towards the top of the weld bead, essentially driving the solidification front in the same direction allowing for epitaxial growth to occur.

Immediately following the extinguishing of the arc, the inert gas is still flowing from the shielding nozzle in order to ensure no contaminants enter the molten metal and oxidize the weld. This gas flowing over the bead moves at a constant velocity and drives convective cooling across the surface of the weld. Additionally, the high temperature of the weld bead gives off radiative heat. Both the radiation and convection negatively impact the solidification direction of the weld from the base of the weld towards the top, and this investigation was conducted in order to

determine the relative magnitude of cooling between these two paths when compared to the conductive heat transfer from the weld into the substrate.

Huang et al. demonstrated the ability to model an impinging jet flow across the surface of a convex bead [16]. While this method was used to analyze heat transfer varying the geometry of the beads (convex vs concave) for the effect of cooling, it also provides great insight into the phenomena that occur directly after the arc is extinguished in the GMAW welding process. Figure 3.1.1 depicts the scenario directly after welding. The jet of inert gas becomes a free jet immediately after it leaves the shielding nozzle and flows perpendicular to the weld bead. After contacting the bead, the free jet is then translated into adherent jets.

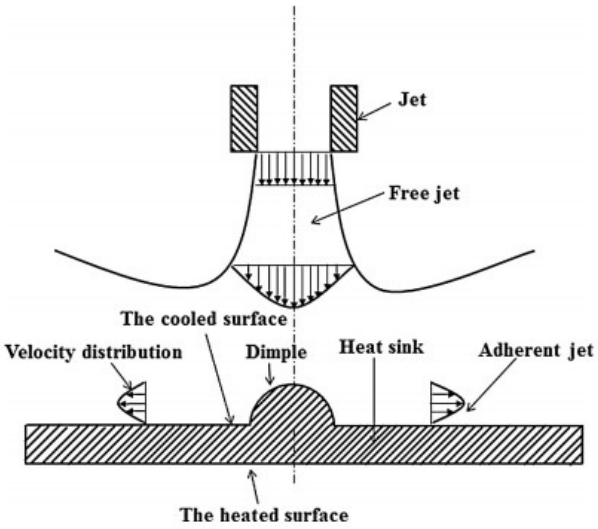

Figure 3.1.1. Impinging Jet Flow diagram [16].

The study conducted by Huang et al. discusses the boundary conditions required to successfully model the fluid flow of a free stream over a convex dimple. The thermal model in the current study includes four components consisting of the base plate of the welding apparatus, the substrate the weld is deposited on, the weld bead itself, and the shielding gas nozzle. Although the weld bead and the substrate were modeled as separate pieces, they were thermally coupled in this study to mimic the conductive heat transfer occurring from the weld bead into the substrate. This model takes into account an initial fluid velocity at the inlet boundary (the gas nozzle), a relative outlet boundary condition of 0 psi (ambient surroundings), symmetry in the X and Y planes, and the rest of the parameters for the Solidworks simulation can be found in table 3.1.1.

Table 3.1.1. Solidworks Thermal Simulation Parameters

Parameter	Value	Units
Substrate diameter	25	mm
Weld bead diameter	5	mm
Gas flow rate	1.862	m/s
Nozzle stickout from surface	8	mm
Initial weld bead temperature	1650	°C
Emissivity	.2	-

Unless otherwise specified, all physical property values used were for Ni-200 in the substrate and were given ambient initial condition values at 25°C, 101.325 kPa. An emissivity of .2 was chosen as a result of the findings of Teodorescu et al. on ultra-pure nickel specimens at high temperatures [17]. Results of this study were then used to determine if the cooling of the deposit would be appropriate for promoting directional solidification. Once this portion of the analysis was completed, a particle study was also conducted to ensure that particle paths of the shielding gas aligned with the anticipated paths based on the physical setup. Upon validation of the previous two methods, numerical results were then analyzed using data gained from both the thermal study as well as the particle study.

3.2 Equipment

Physical experimentation was conducted on two machines unique to the University of Idaho, the Vandalforge which is a GMAW WAAM machine and the UI-GTAAM which is a GTAW WAAM machine. Parameters critical to weld quality include travel speed, wire feed speed, current, stickout, and shielding gas flow. These parameters were determined experimentally for both machines prior to this study to ensure proper fusion and material deposition were achieved.

Vandalforge

The Vandalforge is a custom WAAM apparatus developed at the University of Idaho utilizing a commercially available MIG welding power supply (Miller Dialarc 250) coupled with a custom motion system capable of moving the print head in the Z and X directions, while the print bed moves in the Y direction. These motions are driven via stepper motors controlled by a Smoothie X5 control board flashed with custom firmware to control the stepper motors. GCODE is sent to the control board using a customized version of OctoPrint as the graphical user interface (GUI). In addition to controlling the motion system, the GCODE sent to the controller also

regulates other parameters such as wire feed speed, shielding gas flow initiation, arc initiation and travel speed. Figure 3.2.1 depicts the physical hardware of the VandalForge system in its entirety.

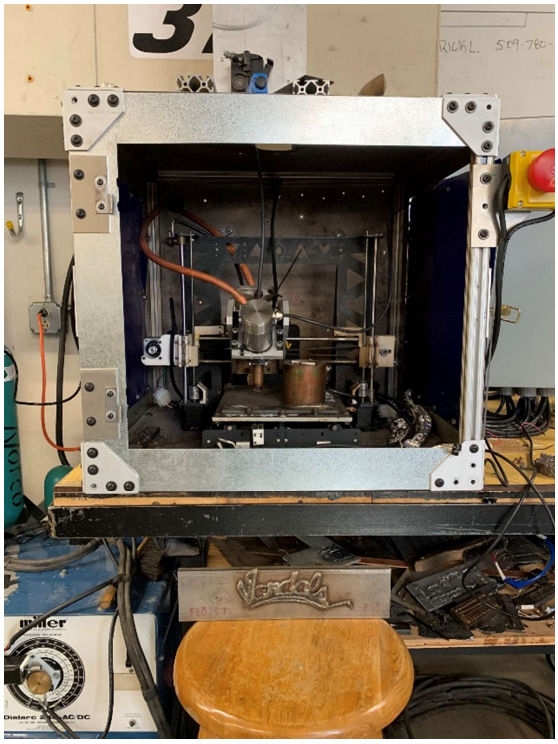

Figure 3.2.1. Picture of the Vandalforge WAAM system

Another parameter critical to deposit characteristics is the stickout distance from the contact tip to the substrate shown in figure 3.2.2. The GMAW process utilizes a contact tip as an electrode that transfers electrical current through the wire causing the wire to be the site of the arc initiation. Previous experimentation determined that a higher stickout causes a taller, narrower bead and a shorter, wider bead for shorter distances. For the experiments performed in this research, a stickout distance was chosen to create a hemispherical weld bead.

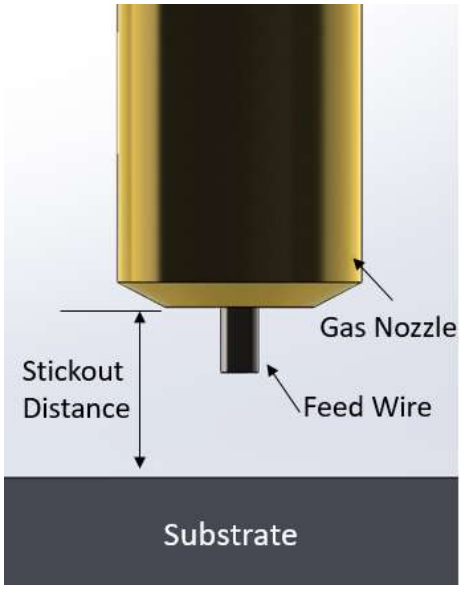

Figure 3.2.2. Diagram of VandalForge welding interface demonstrating measured stickout distance

UI-GTAAM

The UI-GTAAM is a custom TIG WAAM machine that was developed at the University of Idaho utilizing a commercially available TIG power supply (AHP Alphatig 200x) coupled with a custom motion gantry system like the Vandalforge. Unlike the Vandalforge, the print bed is stationary, and the motion system is responsible for moving the print head in all three directions. A Smoothie X5 controller is used in a similar manner as the VandalForge to control the motion system via stepper motors by executing commands delivered by GCODE. The arc is initiated by a foot pedal manipulated manually, and the wire feed system consists of a stepper motor controlled by an Arduino Uno with the stepper motor speed mapped from the analog reading of a potentiometer, enabling the wire feed speed to be adjusted rapidly by the user during deposition. Shielding gas flow is initiated at the moment the foot pedal is depressed via a gas solenoid located in the power supply. The UI-GTAAM machine is shown in Figure 3.2.3.

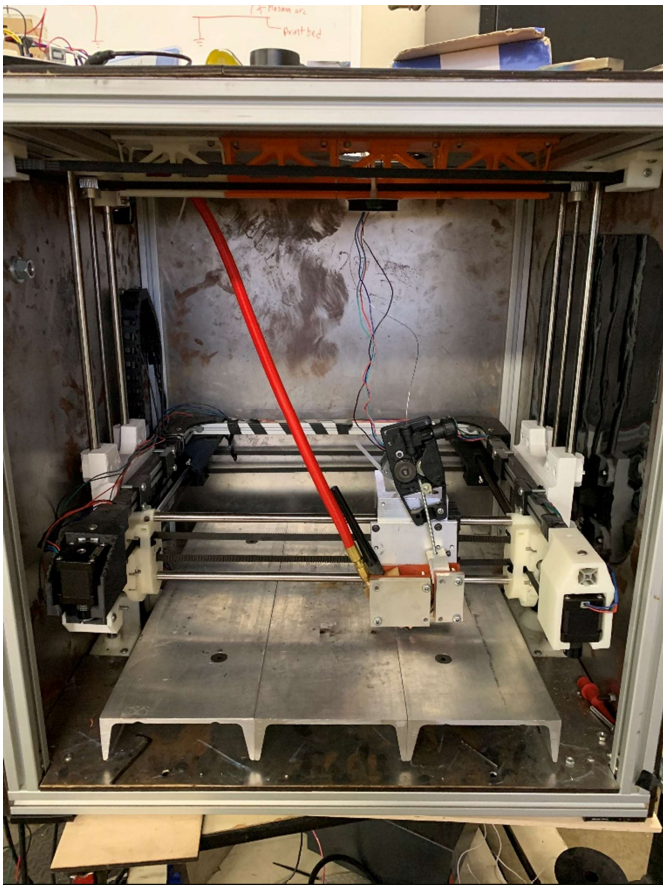

Figure 3.2.3: Picture of the UI-GTAAM machine

Unlike the VandalForge system, the stickout length of the UI-GTAAM machine is defined as the distance from the tip of the tungsten electrode to the substrate. While this parameter does not directly affect the shape of the deposited weld bead as much as in the VandalForge system, it is a critical parameter to ensure proper alignment of the wire being fed into the molten weld puddle. Too much stickout causes the wire being fed into the arc to directly disrupt the arc and cause puddle instability, and too little stickout causes the wire to approach the substrate at too shallow of an angle resulting in premature melting of feed wire and disruption of the feeding process. Additionally, the distance between the tip of the tungsten and the bottom of the gas shielding cone must be carefully maintained at a distance long enough for the shielding nozzle to clear the substrate during travel but short enough that the shielding gas pocket provides sufficient shielding from atmospheric contamination that may lead to arc instability or impurities such as voids.

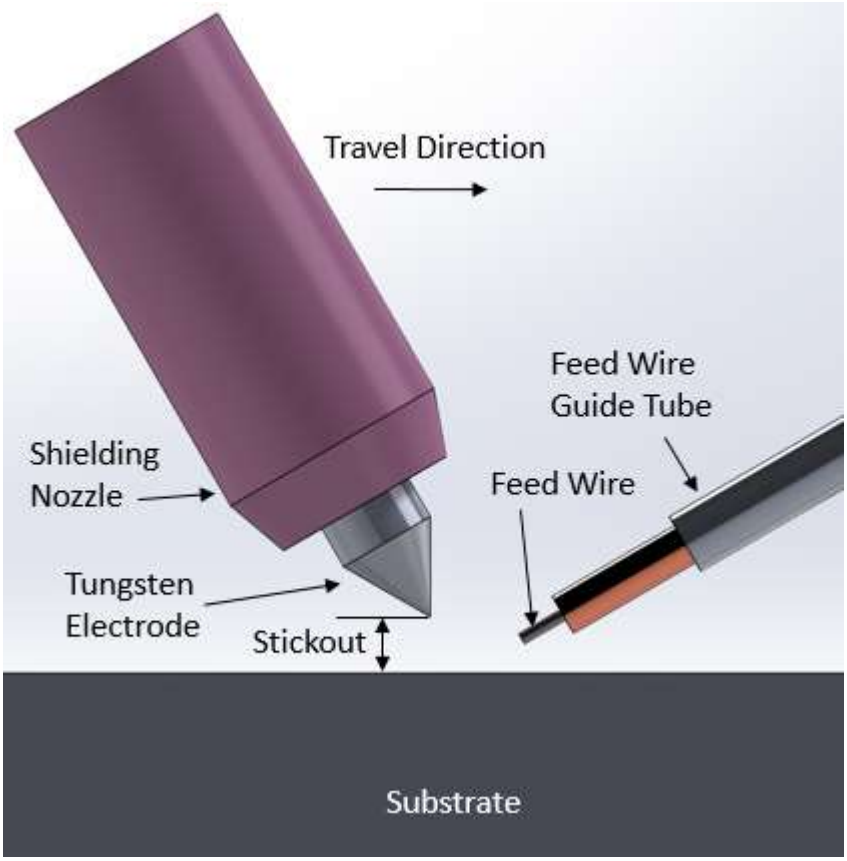

Figure 3.2.4. Diagram illustrating the UI-GTAAM torch and wire feed interface as well as stickout distance

3.3 Printing

Ideal physical experiment parameters were obtained previously by extensive trial runs with both machines. The combinations of the parameters affect not only the quality of the weld, but there is a narrow window for the weld to have proper penetration as well as porosity avoidance without the arc "burning through" the thin single crystal substrate. Initial experiments were conducted with the VandalForge on a piece of ultra-pure zone refined nickel obtained as the result of a prior experiment with grain boundaries large enough to be clearly visible to the naked eye (roughly 5mm in diameter), and later experiments were conducted on a 99.995% pure single crystal specimen oriented in the [111] direction. Table 3.3.1 contains a description of each test, what machine was used, and the type of deposit made. The wire used in both machines was .020 inch diameter tempered Ni-200 wire, the composition of which may be found in Appendix A: Ni-200 Composition. The shielding gas used in all experiments was pure Argon. Wire was wiped down with isopropyl alcohol immediately before each run was conducted.

Table 3.3.1. Overview Table of Experiments Conducted

Experiment	Machine Used	Type of Deposit	Substrate
Preliminary	VandalForge	Spot	Zone Refined Nickel (Figure 3.3.1)
Preliminary	VandalForge	Spot	Single Crystal
A,B,D,E	UI-GTAAM	Continuous Bead (50mm)	Single Crystal
C	UI-GTAAM	Spot	Single Crystal

Vandalforge

In conjunction with the thermal design, experimentation was conducted with a GMAW process on a small piece of zone refined pure nickel with grains large enough to be visible to the naked eye. This is shown in figure 3.3.1.

Figure 3.3.1. Zone refined nickel with visible gran boundaries next to a US quarter for size comparison.

A region on the sample was located that contained a grain with a diameter of roughly 5mm to perform a spot weld on. A spot weld was performed in this location with an initiated arc lasting for two seconds, one second with wire being fed and then purely the contact tip maintaining the arc. Using the contact tip to maintain the arc stems from the thermal analysis and the principle of directional solidification. Maintaining the arc after wire feed halts allows for a slower cooling rate on the surface of the weld, the region hypothesized to cool faster than the time

required for the solidification front to travel from the substrate upwards. Additional welding parameters are listed in Table 3.3.2.

Table 3.3.2: Experimental parameters for Vandalforge spot welds

Parameter	Value	Units
Wire Feed Speed	23.47	m/min
Voltage	30	V(DC)
Current	165	A
Gas flow rate	14.16	L/min
Nozzle stickout from surface	8	mm
Pre Weld Gas Purge Time	1	Second
Post Weld Gas Purge Time	2	Seconds

Once the initial weld was performed on the sample piece of zone refined nickel, the same parameters were used to deposit a spot weld on the piece of single crystal substrate oriented in the <111> direction.

UI-GTAAM

In preparation for deposition on the UI-GTAAM, optimal welding parameters were again obtained through extensive experimentation. In all experiments, a 2% Lanthanated tungsten electrode was ground to a 60° angle at the tip and the torch was held at an angle of 60° from with the substrate surfaces as recommended from the findings of a study conducted by Gokhale et al.[18]. Wire was fed into the arc at a 90° angle from the torch orientation at an elevation of .25 cm below the tip of the electrode. Further experimental setup parameters are illustrated in Figure 3.3.2.

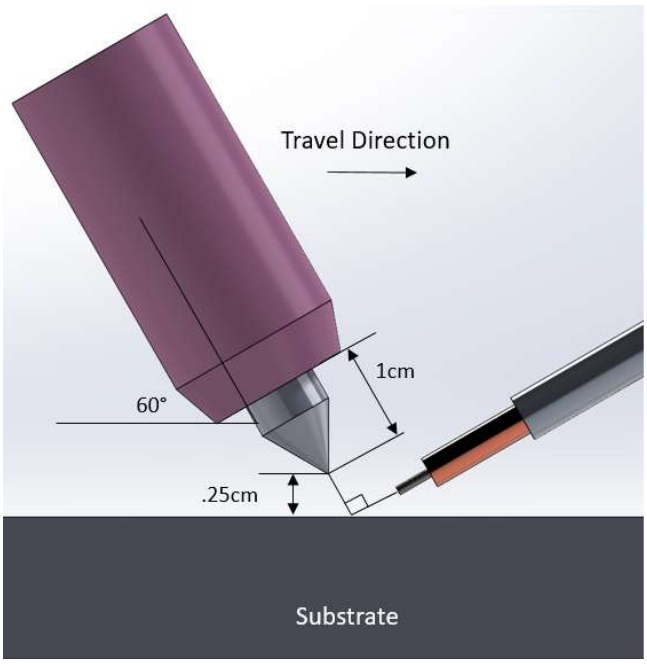

Figure 3.3.2. Experimental values and orientation for torch setup on UI-GTAAM.

A window of welding parameters that yielded successful deposition was modeled using an adaptation of Prado-Cerqueira et al.'s method modified to include the feed speed of wire with a given diameter. It was experimentally determined that at a fixed current, stickout, torch orientation, wire feed orientation, and gas flow rate, wire feed speed and travel speed must be inversely related in order to maintain acceptable weld beads. After initial parameters to deposit material were determined by extensive testing on grade 304 stainless steel, Prado-Cerqueira et al.'s model was altered to include wire feed speed on a linear travel rate for the .020" wire used in this experiment. Initially, travel speed was varied at a constant current to find the maximum travel speed that could be achieved while maintaining a puddle in the arc. Next, wire feed speed was varied to find the maximum wire feed speed allowable to ensure consistent welds while keeping arc and puddle stability. Next, a ratio was derived between current and wire feed speed to provide insight to optimal welding parameters when utilizing the UI-GTAAM. This ratio provides the optimized window of the highest rate of material deposition while ensuring quality, void-free welds and is summarized by:

$$Current/Feed\ ratio = \frac{A}{v_{wire}} \tag{4}$$

Where A is the current v_{wire} is the feed speed of the wire. At 55A, the experimentally determined required amperage to maintain a consistent puddle at a travel speed of 200 mm/min, the maximum wire feed speed achieved while maintaining weld quality was 12.7 mm/s, yielding a Current-Feed ratio of 4.33. For the purposes of this experiment, current and travel speed were not manipulated once consistent welding parameters were established on the stainless steel, however impromptu changes were required when welding on the single crystal substrate. Initial parameters for the welds are shown in Table 3.3.3.

Table 3.3.3. Initial Welding parameters for UI-GTAAM experiments

Parameter	Value	Units
Wire Feed Speed	12.7	mm/s
Voltage	20	V(DC)
Current	55	A
Travel speed	200	mm/min
Gas flow rate	14.16	L/min
Tungsten stickout from shield cone	6	mm
Nozzle stickout from surface	2.54	mm
Pre Weld Gas Purge Time	1	Second
Post Weld Gas Purge Time	5	Seconds

3.4 Microscopy

Once the samples had been created, the deposits were sectioned with a diamond saw and cold mounted in epoxy. After the epoxy had cured, the samples were sanded with 400 grit, 600 grit, and 800 grit sandpaper, 3μm polishing compound, and then 1 μm polishing compound on a wet platen. Prior to optical microscopy, samples were etched with Marbles reagent per ASTM E3 (Appendix B: Marbles Reagent Composition and Procedure). Once optical microscopy was completed with an Olympus PGM-3 microscope, the first specimen was re-polished and then placed in a vibratory polisher for 24 hours with .05 μm colloidal silica in preparation for electron microscopy to use EBSD to map individual grains and compare to optical microscopy images to validate the etchant. All electron microscopy was conducted on an FEI/Thermo Scios SEM with a Thermo QuasOr EBSD Detector.

Chapter 4: Results

4.1 Numerical Analysis

The particle study of the thermal analysis yielded a particle path that aligned well with the initial findings of Huang et al. as shown in figure 4.1.1 [16].

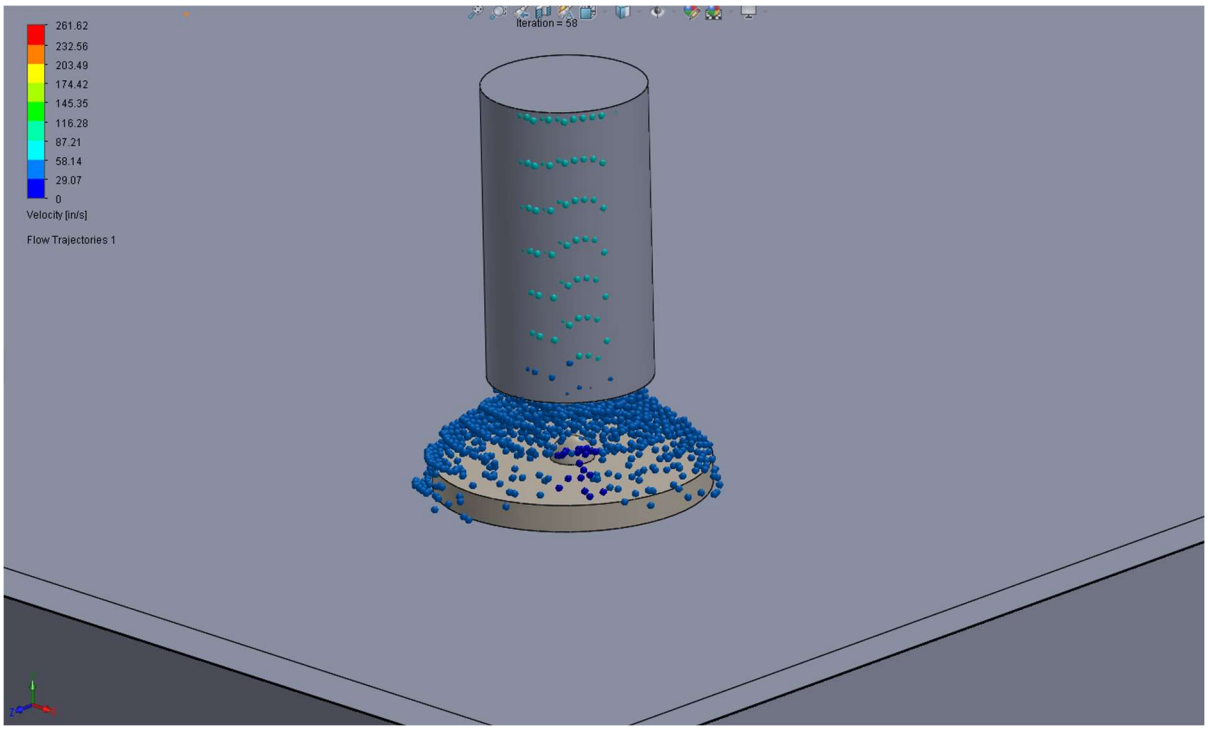

Figure 4.1.1. Particle study results depicting argon flowing over substrate and weld bead.

Once the particle study was completed, the coefficient of convection of the flowing argon was extracted for use in further calculations. The convective coefficient determined from the study was 36.513 $\frac{W}{m^2K}$, while the total surface heat flux for the bead was found to be 28,773.207 $\frac{W}{m^2K}$.

After the particle study yielded proper flow paths to simulate the argon flowing over the weld bead, a transient analysis was performed to study the weld bead over a period of two seconds broken into .01s intervals and a gradient graph was created to compare cooling rates of the surface of the weld to the rest of the weld. Figure 4.1.2 illustrates the thermal gradient of the weld and substrate immediately after the weld is deposited, or the initial case.

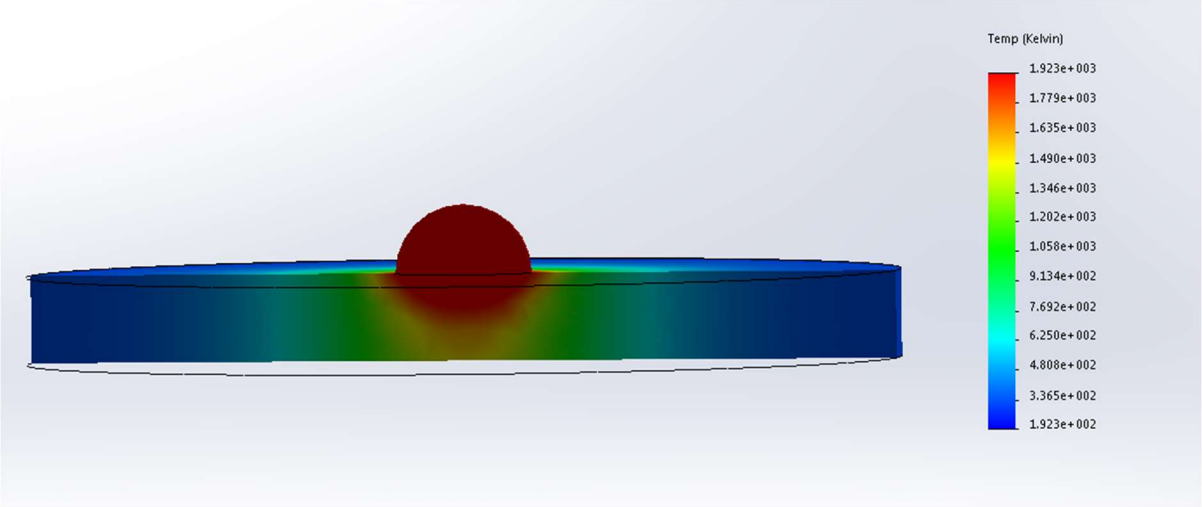

Figure 4.1.2. Thermal Gradient plot of weld bead and substrate immediately after weld is deposited.

4.2 Optical Microscopy

VandalForge Results

Once the spot weld had been deposited onto the piece of zone refined pure nickel, it was then sectioned using a diamond saw and cold mounted in epoxy. Figure 4.2.1 depicts the initial deposit made on the zone-refined nickel substrate as well as the sectioning line that the diamond saw cut.

Figure 4.2.1. Zone refined nickel substrate specimen immediately following deposition of spot weld for one second. The red line illustrates the section line of the diamond saw.

Figure 4.2.2 shows the sample mounted in epoxy after polishing and etching.

Figure 4.2.2. Image of sectioned weld cold mounted in epoxy and polished to 1 micron on a wet platen.

After the specimen had been mounted and polished, it was then etched with Marble's Reagent and optical microscopy images were captured. Images were captured separately and put together using fiduciary marks such as voids and fusion line continuity to achieve macroscopic resolution in a composite image.

Figure 4.2.3. Optical microscopy images taken of WAAM spot weld section on zone-refined nickel specimen after applied etchant.

Once experimentation was performed on the zone-refined nickel, another test was conducted using the single crystal nickel substrate and the same parameters as the previous experiment. Two spot welds were placed next to each other slightly overlapping.

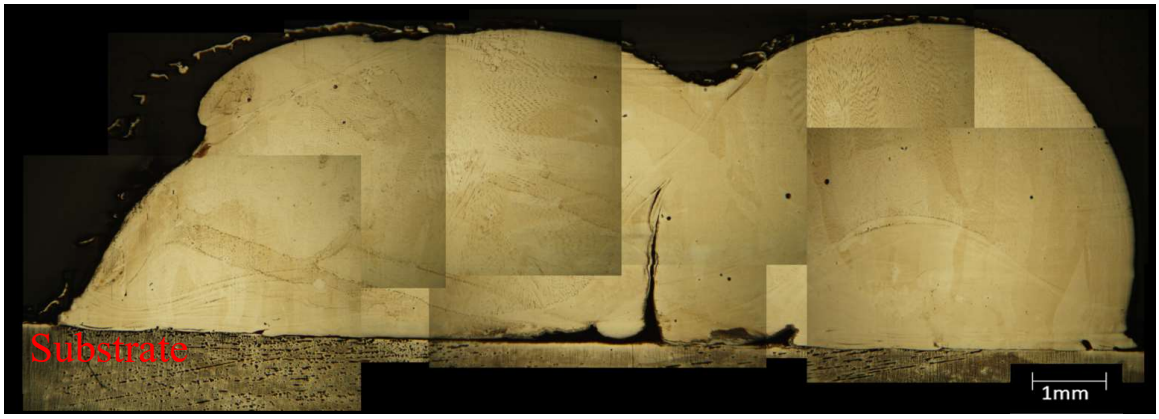

Figure 4.2.4. Optical microscopy results of Vandalforge depositions on single crystal substrate.

UI-GTAAM Results

The welds on the UI-GTAAM were deposited onto the single crystal substrate oriented in the <111> direction. Figure 4.2.5 depicts two different welds, one located along the top edge of the substrate and another on the opposite side of the substrate was deposited after the piece had completely cooled. Weld A was deposited using the parameters outlined in the methods section and the parameters for weld B are found in Table 4.2.1.

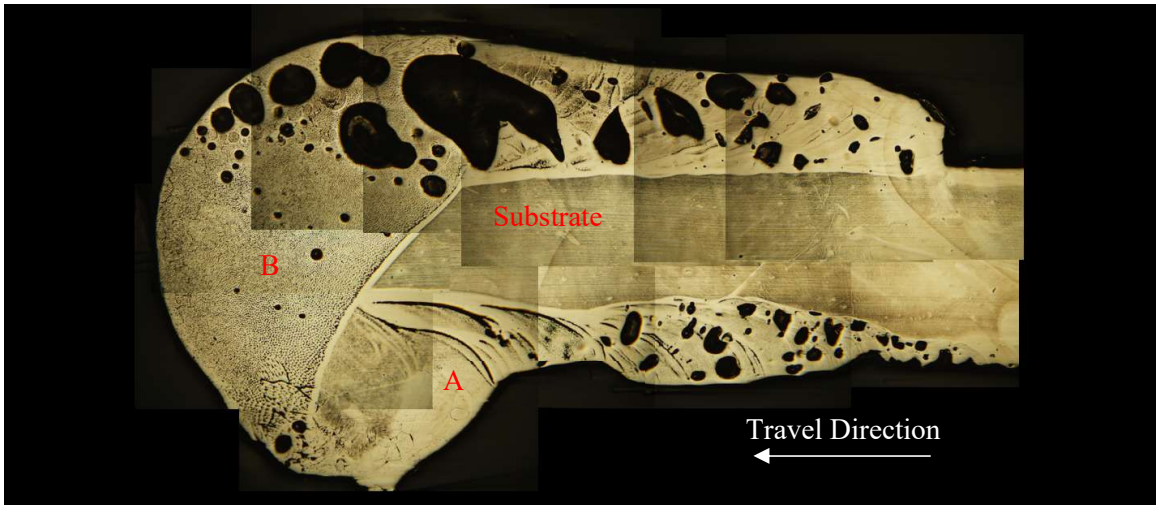

Figure 4.2.5. Optical Microscopy results for UI-GTAAM deposits. Two welds are present, weld A and weld B, with weld B slightly overlapping the tail end of weld A.

Table 4.2.1. Parameters for weld B of UI-GTAAM experiments. Wire feed speed was increased 10% from initial parameters used in weld A.

Parameter	Value	Units
Wire Feed Speed	13.9	mm/s
Voltage	20	V(DC)
Current	55	A
Travel speed	200	mm/min
Gas flow rate	14.16	L/min
Tungsten stickout from shield cone	6	mm
Nozzle stickout from surface	2.54	mm
Pre Weld Gas Purge Time	1	Second
Post Weld Gas Purge Time	5	Seconds
Current-Feed Ratio	3.95	

After welds A and B were performed, parameters were again changed for welds C and D. Figure 4.2.6 illustrates welds C and D again performed on opposite sides of substrate. Weld C was performed with the current dropped to the minimum current required to strike an arc with the substrate. Parameters for welds C and D can be found in Tables 4.2.2 and 4.2.3, respectively.

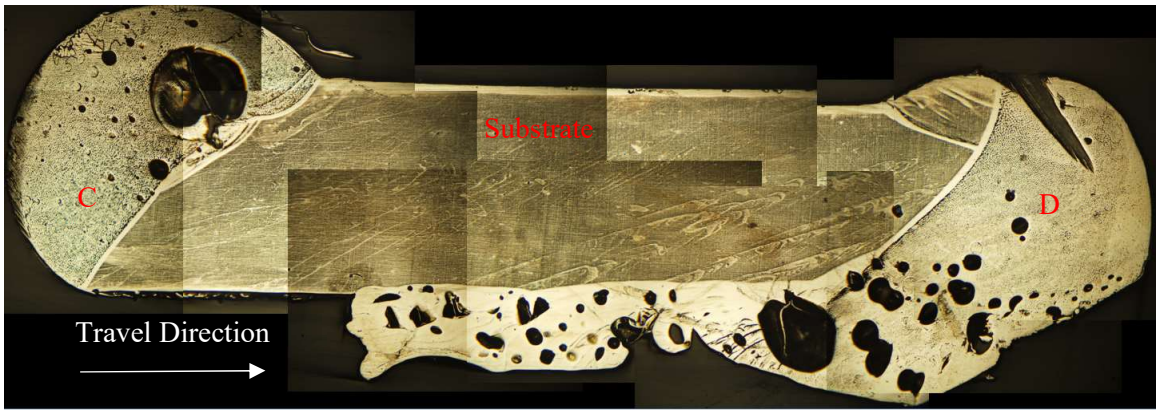

Figure 4.2.6 Welds C and D deposited on single crystal substrate. Weld C is a spot weld with molten material deposited directly onto substrate. Weld D is a weld traveling from left to right.

Table 4.2.2. Welding parameters for weld C. Current was dropped to the minimum current required to strike an arc with the substrate.

Parameter	Value	Units
Wire Feed Speed	12.7	mm/s
Voltage	20	V(DC)
Current	45	A
Travel speed	200	mm/min
Gas flow rate	14.16	L/min
Tungsten stickout from shield cone	6	mm
Nozzle stickout from surface	2.54	mm
Pre Weld Gas Purge Time	1	Second
Post Weld Gas Purge Time	5	Seconds
Current-Feed Ratio	3.54	

Table 4.2.3. Parameters for weld D. Current was restored to initial welding parameters and wire feed speed and travel speed were reduced by 10%.

Parameter	Value	Units
Wire Feed Speed	10.8	mm/s
Voltage	20	V(DC)
Current	55	A
Travel speed	180	mm/min
Gas flow rate	14.16	L/min
Tungsten stickout from shield cone	6	mm
Nozzle stickout from surface	2.54	mm
Pre Weld Gas Purge Time	1	Second
Post Weld Gas Purge Time	5	Seconds
Current-Feed Ratio	5.09	

For the final experiment conducted with the UI-GTAAM, parameters were altered to create the largest continuous deposit possible. Current was increased to 65A while wire feed speed remained constant and travel speed was reduced by 10%. This resulted in a long continuous bead which was the sectioned along the centerline of the weld and prepared for optical microscopy. It is important to note that the cross section was taken along the centerline of the

weld and not following a continuing line along the substrate. Parameters for this weld can be found in Table 4.2.4.

Figure 4.2.7. Cross section of continuous deposit E.

Table 4.2.4. Welding parameters for final weld.

Parameter	Value	Units
Wire Feed Speed	12.7	mm/s
Voltage	20	V(DC)
Current	65	A
Travel speed	180	mm/min
Gas flow rate	14.16	L/min
Tungsten stickout from shield cone	6	mm
Nozzle stickout from surface	2.54	mm
Pre Weld Gas Purge Time	1	Second
Post Weld Gas Purge Time	5	Seconds
Current-Feed Ratio	5.11	

Chapter 5: Discussion and Analysis

5.1 Thermal Study

Once the thermal study was conducted and values for the convective and radiative losses were found, a comparison was made between the heat loss on the surface of the weld (cooling from the top down) and the heat conducted into the substrate (cooling from the bottom up). Multiplying the values of convective heat transfer of 36.513 $\frac{W}{m^2-K}$ and the overall exposed surface area of .0005 m^2, convective heat losses are calculated at 30.113 W. Additionally, radiation heat transfer may be calculated with the Stefan-Boltzmann relationship:

$$Q = \epsilon\sigma T^4 A \tag{5}$$

Where Q is the heat transfer per unit time, ϵ is the emissivity used in the thermal simulation of .2, σ is the Boltzmann constant of 5.6703E-8 $\frac{W}{m^2K^4}$, A is the surface area, and T is the temperature of the bead immediately following the weld (1650 K). Analysis of this equation results in a radiation heat transfer rate of Q=42.028 W per unit time. Combining convective and radiation heat losses yields a heat transfer of 72.1405 W per unit time.

With the combined total heat transfer from both radiation and convection, they can then be compared to the conduction heat transfer from the weld bead to the substrate. In an ideal scenario (to drive planar solidification as in Figure 2.2.4), the conduction heat transfer would be greater than the heat transferred from convective and radiation methods. The conductive heat transfer is found using Fourier's Law:

$$Q = \frac{kA\Delta T}{d} \tag{6}$$

Where k is the thermal conductivity of nickel in this case (76.1 $\frac{W}{mK}$), A is the surface area in contact with the temperature differential (.0005 m^2), ΔT is the temperature difference between the substrate and the weld bead (1307 K), and d is the depth into the substrate in which heat transfers. Plugging values in for each component and leaving the depth at an arbitrary value of 1, the resulting heat transfer per unit time of conductive methods results in 49.731 W per unit time. While this value is less than the combined value for radiation and convective modes, it is important to note that the thermal conductivity and surface area values are dimensioned in meters. In this experiment, the substrate is on the order of millimeters, automatically making the conduction heat transfer several orders of magnitude larger than that of the combined radiation

and convection modes. Comparison of these modes of heat transfer validates that solidification from the substrate to the top of the weld is the driving direction and that directional solidification principles should apply in the experiments.

5.2 VandalForge

The optical microscopy shows three distinct regions in the first bead deposited on the zone refined nickel substrate. These regions consist of equiaxed, columnar, and single crystal grain growth morphologies. Figure 5.2.1 highlights these distinct regions.

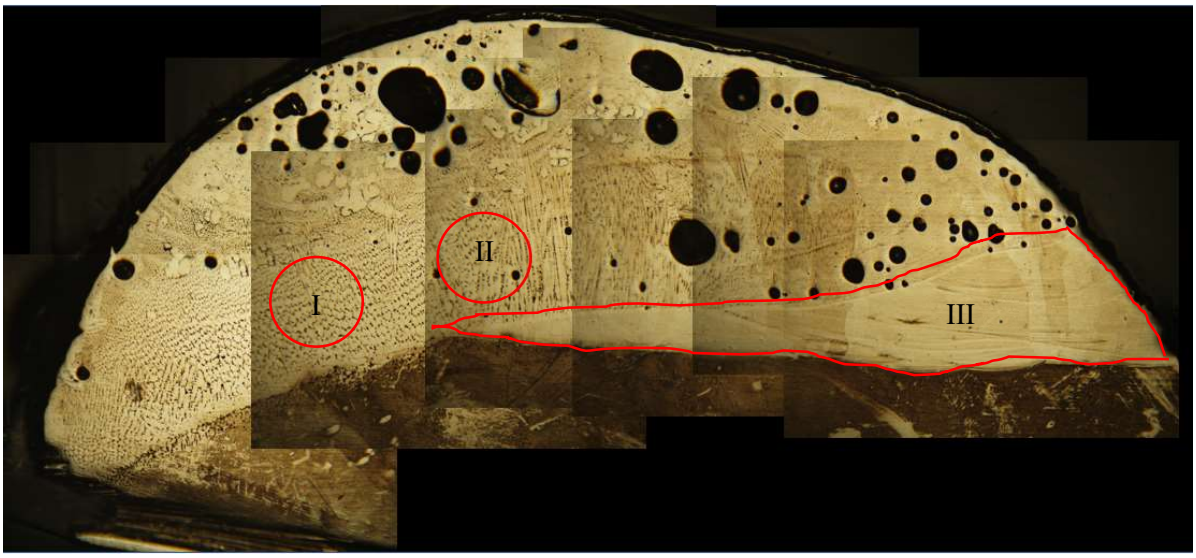

Figure 5.2.1: Optical microscopy with varying grain morphologies identified: Region I containing equiaxed grains, Region II containing columnar morphologies, and Region III containing planar growth.

With these three distinct morphologies present, it can be deduced that different modes of solidification were present in the weld. Analyzing Figure 5.2.1 with respect to Figure 2.2.3, it can be seen that either the solidification rate or the temperature gradient must have varied throughout the weld. The equiaxed grains on the left hand side of Figure 5.2.1 indicates a high rate of solidification as well as a low temperature gradient, whereas the large grained regions towards the right side of the weld indicate slower solidification rate and a higher temperature gradient. This may be explained by the fact that the weld was deposited on the edge of the substrate, creating a larger heat sink on the right side of the weld than the left to conduct heat away from the weld and maintain a higher local thermal gradient in Region III. Upon further examination with increased magnification shown in Figure 5.2.2, there were no visible grain boundaries present in region III as there were in other portions of the deposit.

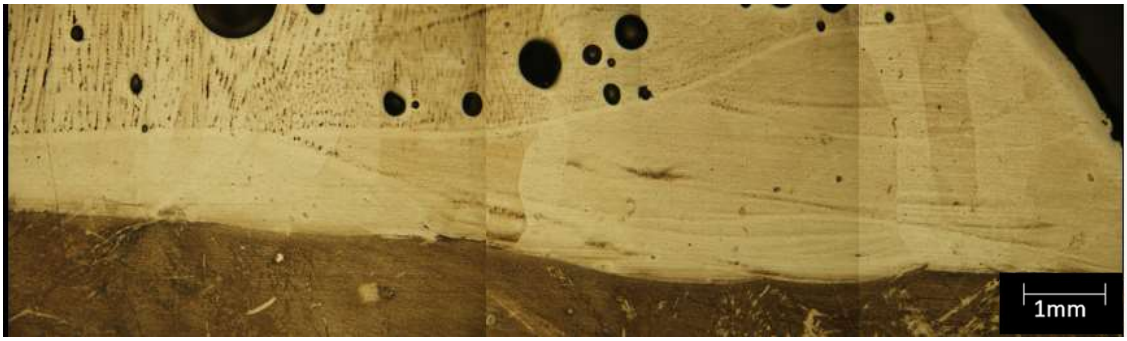

Figure 5.2.2: Enlarged optical microscopy of Region III on the bead deposited on zone refined nickel substrate.

Similar to the initial deposit made on the zone refined nickel piece, optical microscopy on the deposits made on the single crystal substrate presented distinct regions of equiaxed, columnar and suspected planar growth regions as well, with a clear humped boundary present between the planar growth region and the equiaxed region.

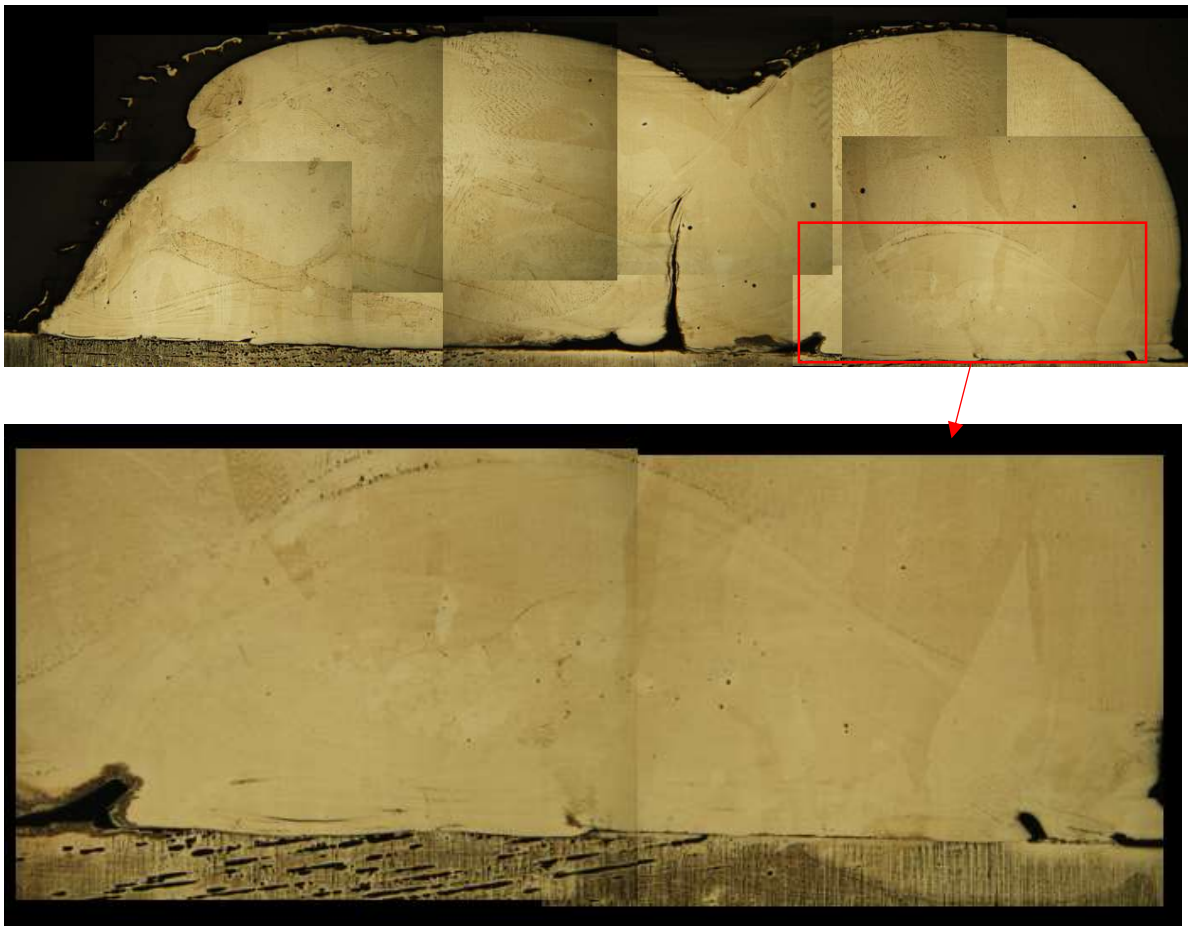

Figure 5.2.3. Magnified image of weld deposited on single crystal nickel substrate. There is a distinct line separating fine grains (top of magnified image) from what appear to be large single grains.

EBSD Analysis

To verify the suspected region of planar growth, the first sample deposited on the zone refined nickel substrate was prepared for EBSD analysis using the University of Idaho's Electron Microscopy lab. Grain boundaries visible via optical microscopy were used as fiduciary marks to ensure the correct region was scanned and the area of interest was within the scanning range. Figure 5.2.4 illustrates the fiduciary marks indicated by the red circles.

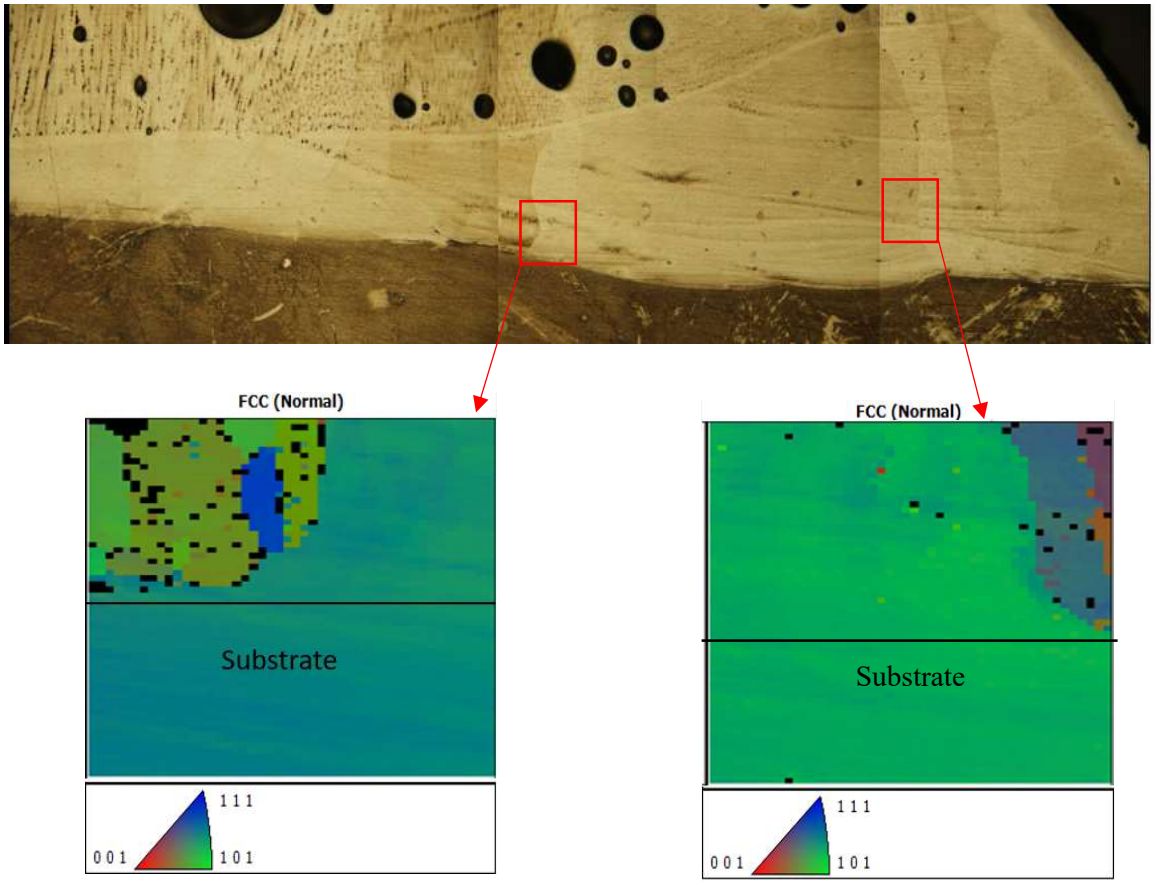

Figure 5.2.4. Fiduciary marks used to mark EBSD boundaries to ensure analysis was performed on the suspected single crystal region of interest and corresponding EBSD maps.

EBSD analysis confirmed that the suspected region of single crystal was all one orientation and that the etchant was effective at highlighting individual grain boundaries. Additionally, the region of deposited material shows no variation from the substrate which indicates epitaxial growth from the substrate. With the EBSD validation of the etchant for suspected grain boundaries large single crystal regions were identified in both GMAW and GTAW type samples. Patterning in the EBSD scans had >99.5% success.

5.3 UI-GTAAM

Upon optical microscopy analysis of the UI-GTAAM samples, regions of single crystallinity were apparent in areas of the weld that had consistent travel and deposition along the substrate despite voids being prevalent within the bead. Figure 5.3.1 is a micrograph of weld A with large crystal regions present at the beginning of the weld (right) as well as large visible grain boundaries in the beaded region of the weld. These large crystal regions are accompanied by

voids resembling beach marks commonly seen in fatigue analysis but can be attributed to the movement of the torch across the substrate combining microvoids as the weld puddle travels with the torch head.

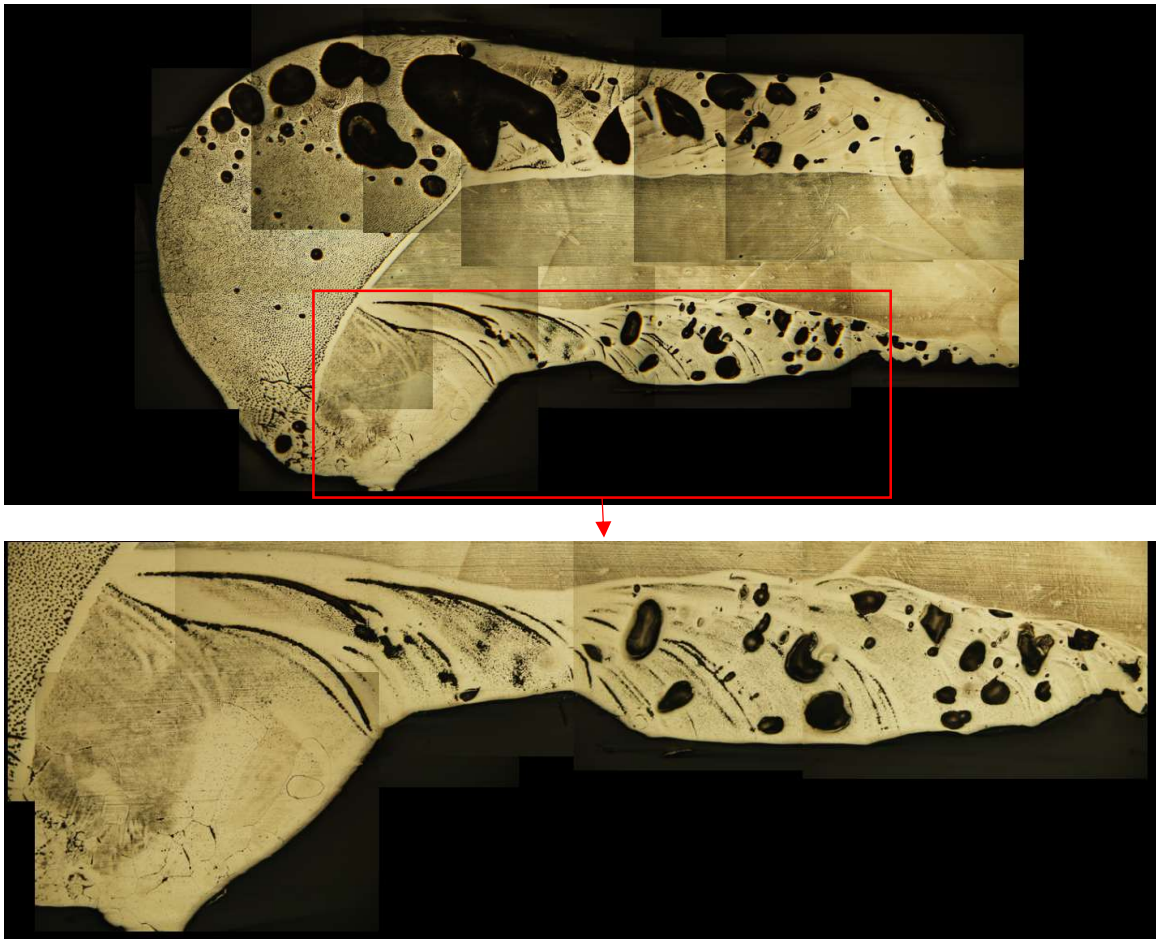

Figure 5.3.1. Magnified image of weld A on the first UI-GTAAM specimen. No grain boundaries are visible along the right side of the weld (initial start) until the deposited material beaded up (left side).

It is worth noting the difference in morphology between welds A and B due to the increase in wire feed speed. In weld B, the end of the weld exhibits a significantly higher amount of equiaxed morphology than that of the end of A which can be explained by the advanced rate of solidification with a higher amount of mass present. For these equiaxed grains to be present, the higher amount of molten metal present must drive the local temperature gradient down far enough below the G/R ratio line to void the possibility of a planar solidification front.

Weld C was an attempt to mimic a process similar to that which is found in the CZ process outlined in Section 2.2.2. Welding parameters were modified to the point where molten wire would bead up on the feed wire before dropping onto the substrate while power input to the

work was kept at the minimum current required to maintain an arc with the substrate. The purpose of attempting this method was to keep the temperature gradient between the substrate and the deposited material as high as was possible, however the entirely equiaxed microstructure indicates that the solidification rate caused by this method of deposition must have drastically outweighed the factor of thermal gradient and caused the deposited material to solidify ahead of the planar solidification region. This mechanism is synonymous with the limited speed of retraction rates in the CZ process, where withdrawal of the seed crystal that is too rapid can lead to stray grain formation [4].

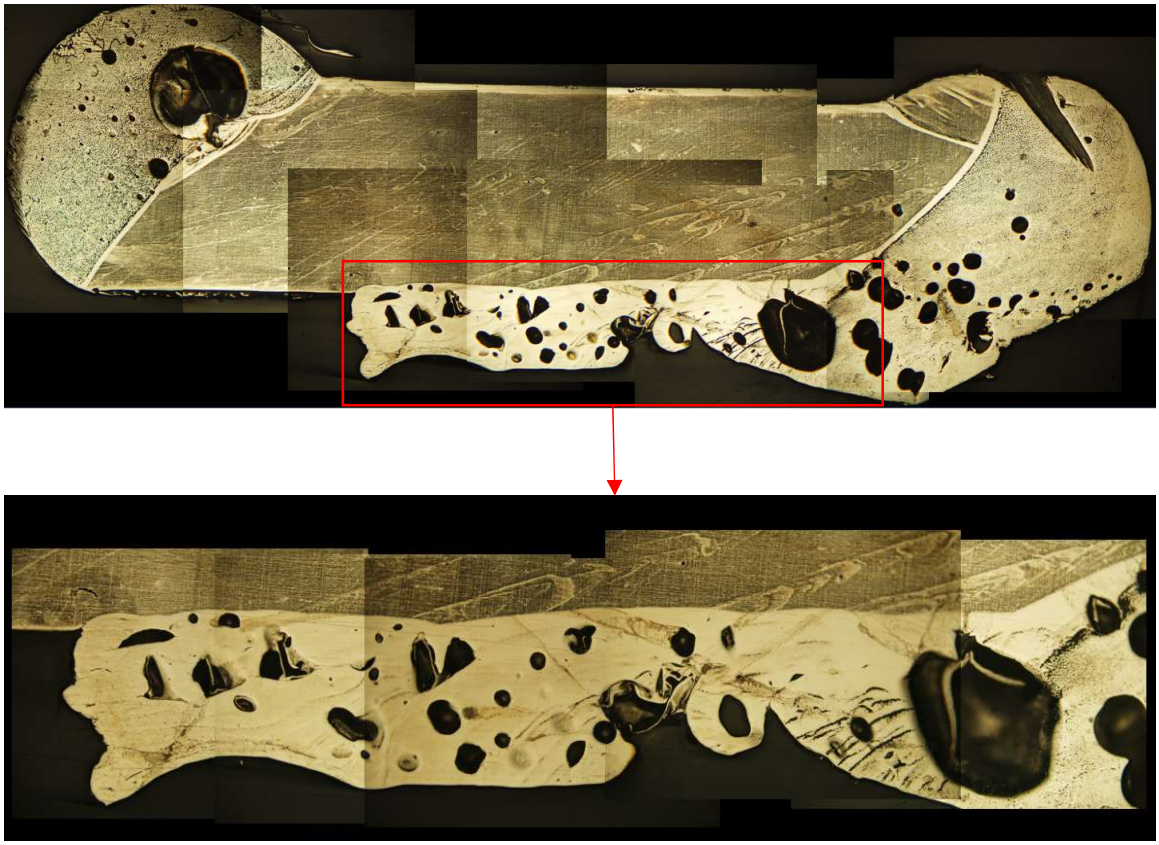

Figure 5.3.2: Weld section containing welds C and D. Weld C is located at the top left corner of the upper picture and contains fine, equiaxed grains. Weld D is located in the bottom right of the upper picture and magnified image is displayed below.

Upon reduction of both wire feed speed and travel speed from initial parameters for weld D, the weld became much more uniform with respect to height and void concentration, especially in the beginning of the weld. Optical microscopy results showed a large region of single crystal that had formed in the beginning of the weld despite a small concentration of voids, with

equiaxed grains forming towards the termination of the weld. These equiaxed grains present at the termination of the weld is consistent with the findings of welds A and B, where the decrease in local temperature gradient after prolonged power input into the substrate is suspected to drive the solidification parameters below the planar solidification region.

In the final experiment conducted on the UI-GTAAM parameters were altered to values that showed consistent, continuous beads similar to welds seen created with the GMAW process. Figure 5.3.3 illustrates the magnified region of interest in this weld.

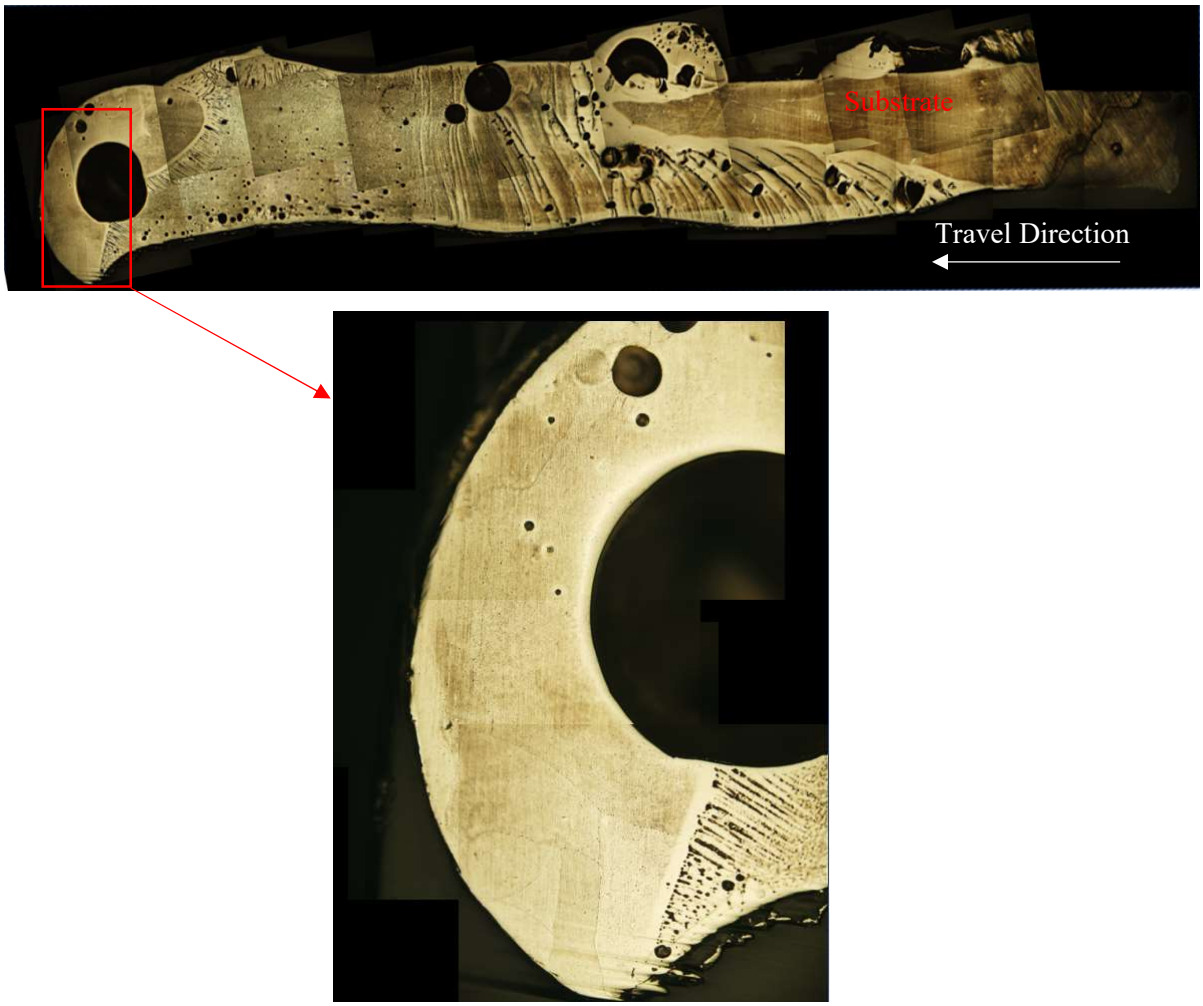

Figure 5.3.3. Final experimental weld conducted on UI-GTAAM with parameters modified to allow for less voids and a thicker deposit. Magnified region is at the termination of the weld in which large grain boundaries are visible surrounding a large void.

While multiple morphologies are again present in this weld, the termination of the weld exhibits a microstructure similar to the single crystal regions present in the VandalForge specimens closest to the substrate. At the beginning of the weld, the microvoid curves present in

all previous experiments are present in regions displaying large crystalline features. As the weld progressed across the substrate, the solidification transitioned from single crystal to equiaxed, indicative of the reduction of local thermal gradient due to prolonged heat input to the substrate. At the termination of the weld, however, there is a distinct transition back into a planar regime as seen in Figure 5.3.3. This can be attributed to the presence of the large void immediately adjacent to the solidifying metal. In this region, local thermal conductivity of the material surrounding the solidifying weld must be substantially lower than that of regions lacking voids due to the lower thermal conductivity of the gasses trapped in the welds. This lowering of thermal conductivity would essentially trap heat in this region of the weld for an extended amount of time, causing the solidification rate locally to be much slower than that of other regions of the weld.

5.4 Voids

In the experimental results derived from both the VandalForge and UI-GTAAM devices, there are a high concentration of voids present in the deposited material. While these are undesirable from a mechanical standpoint, these are likely to stem from a lack of alloying agents in the materials being welded as well as the absence of a flux. Traditionally, alloying elements such as silicon and manganese are provided in the filler wire to decrease the viscosity of the weld pool and enabling trapped gasses and other impurities to diffuse away from the liquid-solid interface and leave the weld uncontaminated [19]. However, with the inclusion of these additional materials such as silicon and phosphorus, the dilemma of constitutional supercooling comes into play when trying to promote planar growth. It is highly probable that the inclusion of these alloying materials would lead to random nucleation sites ahead of the solidification front and inhibit planar growth. Therefore, the nature of these experiments prohibits the use of any form of alloying material to help diffuse contaminants or trapped gasses out of the weld pool and the voids present in these experiments are likely the result of trapped shielding gasses. This lack of alloying material is also suspected in causing the need to alter welding parameters in situ on the single crystal substrate after optimizing welding parameters on stainless steel. Alloying agents in the stainless steel most likely contained trace amounts of the aforementioned elements to assist with the diffusion of welding gasses and impurities as well as decreased the molten viscosity of the weld pool ensuring consistent fluidity.

While voids are impurities that may detract from physical performance, there is an interesting phenomenon that has been observed in these experimental results. In all regions that displayed planar solidification, voids were also present. Traditionally, voids may be viewed as nucleation sites for stray grain formation as molten metal is required to solidify without any

epitaxial scaffolding. However, these voids also lower the local thermal conductivity of the molten surroundings which causes a decrease in solidification rate which is beneficial for achieving planar growth. This can be seen most clearly in Figure 5.3.3, where the termination site of the weld most commonly associated with equiaxed growth transitioned back into a single crystal morphology with very large grain boundaries present.

Chapter 6: Summary and Conclusions

Summary

Single crystal materials are necessary in the expanding field of mechanical components subjected to high thermal and mechanical strain for their outstanding resistance to mechanical creep and corrosion. Nickel superalloys are ideal candidates for these environments due to high melting temperatures as well as corrosion resistance. Current production methods are time consuming and expensive, with repair of damaged components limited to small regions and subject to cracking or loss of ideal microstructural properties. Additionally, directional solidification processes limit the complexity of geometry that is available for mass manufacturing.

Directional solidification processes rely on the theory of epitaxial growth, in that molten metal tends to solidify with grains oriented in the same direction as the substrate. To avoid constitutional supercooling, local temperature gradient must be kept very high and solidification rate must be controlled at a slow rate. Deviation from these parameters may lead to equiaxed morphologies due to different constituents of an alloy solidifying ahead of the solidification front and acting as nucleation sites for stray grains.

Additive manufacturing provides an alternative method of creating components with complex geometry, minimal waste, and relatively rapid rates of deposition and production. WAAM deposits material with the highest rate of material when compared to other forms of additive manufacturing, however the violent nature of the GMAW process leads to unpredictability in arc stability, lack of uniformity in microstructure of welds, and is difficult to accurately model and predict. In addition to these difficulties, welds often cool at a rate several orders of magnitude above traditional directional solidification techniques, stressing the importance of maintaining control of welding and cooling parameters. A variant of GTAW that uses a non-consumable tungsten electrode is a much more consistent and predictable method of material deposition once optimal parameters have been determined for the process. This study

utilized two different machines to conduct experiments on, the VandalForge (WAAM) and the UI-GTAAM (GTAW variant).

Conclusions

In this study, it was found that principles of directional solidification could be applied in both GMAW and GTAW processes of additive manufacturing and it is possible for regions of single crystal to be deposited on single crystal substrates. GMAW processes yielded distinct regions of single crystal, columnar, and equiaxed grains, with planar growth occurring in a region of the highest local thermal gradient and slowest solidification rate. A further comparison of welding parameters was conducted with the UI-GTAAM machine while varying current and wire feed speed. Prado-Cerqueira et al. demonstrated that distinct variations in microstructure of welds were dependent upon parameters such as power, travel speed, and machine efficiency. However, this model did not take into account wire being fed into the weld pool from an external source. Instead, this study compared current to wire feed speed in a simple ratio while keeping all other parameters fixed. It was found that an increase of the Current-Feed Ratio led to more favorable outcomes of single crystal deposition, especially towards the initiation of the weld. However, at higher currents equiaxed grains began to form due to the loss of a high local thermal gradient after a high temperature gain of the substrate with the prolonged power input from the arc. A larger substrate would help limit this local temperature gradient loss by acting as a heat sink. It was also found that clean wire and substrate were critical to ensure consistent arc formation.

Chapter 7: Future Work

Future work in this field should consist of the application of a sufficient heat sink (or larger substrate) to transport heat away from the weld pool at a high enough rate to maintain a thermal gradient that would allow for planar growth to still occur. A larger single crystal substrate would act as an ideal heat sink as well as allow for additional testing.

The addition of an alloying agent would be ideal to decrease the occurrence of voids due to the viscosity of the pure substance, however the principle of constitutional supercooling would most likely prohibit the use of any other external materials in the weld pool. Future experiments could be conducted with a metal with a lower molten viscosity.

References

1. Prajapati, Ashish & Rajpurohit, Shilpesh. (2017). FORMATION AND APPLICATIONS OF SINGLE CRYSTAL MATERIAL. https://www.researchgate.net/publication/322117179_FORMATION_AND_APPLICATIONS_OF_SINGLE_CRYSTAL_MATERIAL
2. https://www.machinedesign.com/mechanical-motion-systems/article/21836518/singlecrystal-turbine-blades-earn-asme-milestone-status
3. Pan, D., Xu, Q., Liu, B., Li, J., Yuan, H., & Jin, H. (2010). Modeling of grain selection during directional solidification of single crystal superalloy turbine blade castings. JOM, 62(5), 30–34. https://doi.org/10.1007/s11837-010-0074-y
4. C. Barry Carter, M. Grant Norton, Ceramic Materials: Science and Engineering, Springer, 2013, ISBN: 978-1-4614-3522-8, DOI: 10.1007/978-1-4614-3523-5
5. Lee, Y., Nordin, M., Babu, S., & Farson, S. (2014). Effect of Fluid Convection on Dendrite Arm Spacing in Laser Deposition. Metallurgical and Materials Transactions B, 45(4), 1520–1529. https://doi.org/10.1007/s11663-014-0054-7
6. David, S., Babu, A., & Vitek, J. (2003). Welding: Solidification and microstructure.
7. Fu, H., & Geng, X. (2001). High rate directional solidification and its application in single crystal superalloys.
8. Henderson, M. B., Arrell, D., Larsson, R., Heobel, M., & Marchant, G. (2004). Nickel based superalloy welding practices for industrial gas turbine applications.
9. Gurtner, F., & Edgewood Arsenal MD. (1969). WHAT IS WELDING. Retrieved from http://www.dtic.mil/docs/citations/AD0695614
10. Kou, S. (2003). Welding Metallurgy. Hoboken, NJ, USA: John Wiley & Sons, Inc. https://doi.org/10.1002/0471434027M.
11. Williams, S. W., Martina, F., Addison, A. C., Ding, J., Pardal, G., & Colegrove, P. (2016). Wire + Arc Additive Manufacturing. https://doi.org/10.1179/1743284715Y.0000000073
12. José Luis Prado-Cerqueira, Ana María Camacho, José Luis Diéguez, Álvaro Rodríguez-Prieto, Ana María Aragón, Cinta Lorenzo-Martín, & Ángel Yanguas-Gil. (2018). Analysis of Favorable Process Conditions for the Manufacturing of Thin-Wall Pieces of Mild Steel Obtained by Wire and Arc Additive Manufacturing (WAAM). https://doi.org/10.3390/ma11081449
13. Gregori, A., & Bertaso, D. (2007). Welding and Deposition of Nickel Superalloys 718, Waspaloy and Single Crystal Alloy CMSX-10. https://doi.org/10.1007/BF03266607

14. Basak, A., Acharya, R., & Das, S. (2016). Additive Manufacturing of Single-Crystal Superalloy CMSX-4 Through Scanning Laser Epitaxy: Computational Modeling, Experimental Process Development, and Process Parameter Optimization. https://doi.org/10.1007/s11661-016-3571-y
15. Fu, H., & Geng, X. (2001). High rate directional solidification and its application in single crystal superalloys. https://doi.org/10.1016/S1468-6996(01)00049-3
16. Huang, X., Yang, W., Ming, T., Shen, W., & Yu, X. (2017). Heat transfer enhancement on a microchannel heat sink with impinging jets and dimples. International Journal of Heat and Mass Transfer, 112, 113–124. https://doi.org/10.1016/j.ijheatmasstransfer.2017.04.078
17. Teodorescu, G., Jones, P., Overfelt, R., & Guo, B. (2006). High temperature, spectral-directional emittance of high purity nickel oxidized in air. Journal of Materials Science, 41(21), 7240–7246. https://doi.org/10.1007/s10853-006-0914-x
18. Gokhale, N. P., Kala, P., & Sharma, V. (2019). Thin-walled metal deposition with GTAW welding-based additive manufacturing process. https://doi.org/10.1007/s40430-019-2078-z
19. Kim, J., Lee, B., & Sohn, T. (2018). Effect of Compositional Variation in TiO 2 -Based Flux-Cored Arc Welding Fluxes on the Thermo-physical Properties and Mechanical Behavior of a Weld Zone. Metallurgical and Materials Transactions A, 49(7), 2705–2720. https://doi.org/10.1007/s11661-018-4624-1

Appendix A: NI-200 Composition

Table A. Material composition of Ni 200

Material	Chemical Composition %
Nickel	99.0 min.
Copper	.25 max.
Iron	.40 max.
Manganese	.35 max.
Carbon	.15 max.
Silicon	.35 max.
Sulfur	.01 max.

Appendix B: Marble's Reagent Composition and Procedure

Table B. Marble's Reagent Composition

Component	Amount
CuSO4	4g
HCL	20cc
H2O	20cc

Mix all components thoroughly until CuSO4 is completely dissolved in solution. Submerge surface of material to be etched in solution for 20 seconds, then remove and douse sample with DI water to prevent further etching. Repeat as necessary until desired extent of etching has occurred.